Refined and Simplified Simulations for Steel–Concrete–Steel Structures

Robine Calixte, Ludovic Jason, Luc Davenne

applied mechanics

Article

Refined and Simplified Simulations for Steel–Concrete–Steel Structures

Robine Calixte [1,2], Ludovic Jason [1] and Luc Davenne [2,*]

[1] CEA, Service d'Études Mécaniques et Thermiques, Université Paris Saclay, 91191 Gif-sur-Yvette, France; robine.calixte@sitowie.fr (R.C.); ludovic.jason@cea.fr (L.J.)
[2] Laboratoire Energétique Mécanique Electromagnétisme, Université Paris Lumières, 92410 Ville-d'Avray, France
* Correspondence: luc.davenne@parisnanterre.fr

Abstract: Steel–concrete–steel (SCS) sandwich structures have gained increasing interest in new constructions. The external steel plates increase the stiffness, the sustainability, and the strength of the structures under some extreme solicitations. Moreover, the use of these plates as lost prefabricated formwork makes SCS structures modular, enabling higher construction rates. However, for a better understanding of the complex behavior of these structures up to failure, refined numerical simulations are needed to consider various local phenomena, such as concrete crushing in compression and interface interactions. Indeed, the highly non-linear steel–concrete interaction around the dowels is the key point of the composite action. In this contribution, a refined methodology is first proposed and applied on a push-out test. It is especially demonstrated that a regularization technique in compression is needed for the concrete model. Interface elements are also developed and associated with a nonlinear constitutive law between steel connectors and external plates. From this refined methodology, simplified numerical modeling is then deduced and validated. Directly applied to an SCS wall-to-wall junction, this simplified strategy enables the reproduction of the overall behavior, including the elastic phase, the degradation of the system, and the failure mode. The response of each component is particularly analyzed, and the key points of the behavior are highlighted.

Keywords: steel–concrete–steel junctions; push-out test; numerical modeling; refined modeling; regularization in compression; simplified modeling

Citation: Calixte, R.; Jason, L.; Davenne, L. Refined and Simplified Simulations for Steel–Concrete–Steel Structures. *Appl. Mech.* **2023**, *4*, 1078–1099. https://doi.org/10.3390/applmech4040055

Received: 11 September 2023
Revised: 8 October 2023
Accepted: 13 October 2023
Published: 18 October 2023

1. Introduction

Steel–concrete–steel sandwich structures are composite structures made of a concrete core caught between two steel plates [1–3]. The bond between these two components is ensured by a connection system that is responsible for the composite action (Figure 1). Different types of mechanical connection systems exist, such as shear studs [4,5], Bi-steel [6], J-hook connectors [7], or mixing technologies with shear studs and ties, J-hooks and studs [8], etc. The structure provides the advantages of reinforced concrete (specifically, strength and stiffness) thanks to the optimal use of concrete and steel. Moreover, the external steel plates increase the stiffness, the sustainability, and the strength under some extreme solicitations [9–12] and are used as lost formwork, which can be prefabricated. SCS structures are thus considered modular structures [13–15] and are gaining increasing interest in construction.

Initially designed as an alternative solution for the building of submerged tubular tunnels in the mid-1970s [1,2], SCS structures have been gradually used in bridge decks (Figure 2a) [12] for the construction of shear walls in high buildings [16], for submerged tunnels [17,18] and for blast and impact shield walls or liquid and gas containers [3,19]. In the nuclear field, SCS structures have been chosen for the internal structures of the third-generation nuclear power plants "AP1000" [20] (Figure 2b) and "US-APWR" [21].

They are also under consideration for Small Modular Reactors (SMR) or Advanced Light Water Reactors (ALWR) [13].

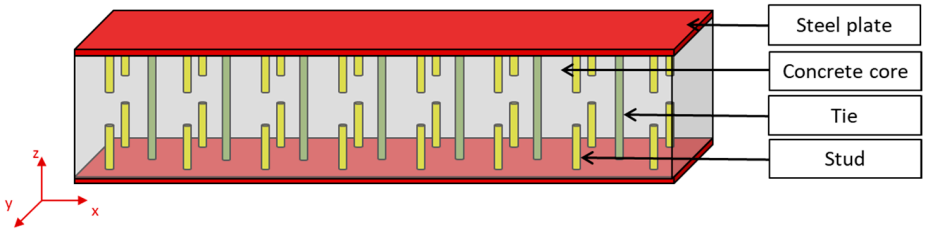

Figure 1. Principle of an SCS beam with studs and ties.

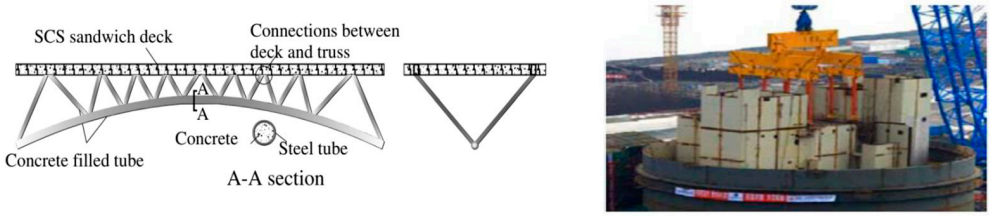

(**a**) (**b**)

Figure 2. Example of (**a**) an SCS sandwich bridge deck [12]. (**b**) AP1000 containment module [22].

The composite nature of SCS structures leads to complex behavior. In fact, the efficiency of SCS structures is directly dependent on the transfer of shear forces between the steel plates and the concrete through the dowels, which is a key point in such structures. Thus, particular attention must therefore be paid to the behavior of the connection system since compression of the concrete around the connectors, deformation or buckling of the steel plate, or shearing of the connectors directly affects this transfer of forces [12,23–26]. These elementary behaviors are generally characterized through push-out tests. As described in (CEN, 2005a), the push-out test is based on the application of a vertical load on a steel beam connected to concrete blocks by the two flanges thanks to a connection system. During the loading, bending and shearing of the connector first appear, combined with a progressive crushing and tearing of the concrete around the connectors [25,27].

In numerical studies, the local nature of these nonlinear phenomena leads to the need for a refined simulation. Several studies propose simulations of the push-out test with 3D solid elements, for example, in [28–32]. The overall stress–displacement curve is generally well reproduced, and failure modes are sometimes identified. But to the best of our knowledge, none of them discuss the mesh-dependency of the results. However, the use of softening models leads to problems of objectivity of results, which have been widely discussed for the simulation of concrete behavior in tension. Different techniques of regularization have been provided [33–35]. In the simulation of concrete-plate dowel connections, the softening behavior of concrete in compression and shear is an additional issue. Techniques like those used in tension can be used, but the compression cracking energy must be identified, which is another issue [36–38].

Although these refined methods allow the simulation of the behavior of test specimens, they are not fully adapted for the simulation of large-dimension structures, for which representative simplifications are needed. Sandwich structures are widely used in various fields of engineering, and a great deal of research has been carried out to develop analytical or numerical solutions, particularly in aerospace engineering [39,40]. But, the technologies used to transfer forces between the skins and the core are different, such as bonding or functionally graded materials [41], avoiding the concentrations encountered around singularities such as studs in SCSs. On the other hand, the calculated non-linearities are large displacements and buckling, whereas the materials have elastic behavior.

In this paper, a refined modeling strategy is first developed, allowing the capture of local behaviors related to SCS composite structures. Compared to a "classical" simulation methodology, particular attention is paid to the mechanical behavior of concrete in compression and to the shear behavior of the connectors. In the second part, a simplified methodology is proposed to reduce numerical costs and enable larger structures to be simulated. It is applied to the behavior of a wall-to-wall SCS junction under bending load. Numerical and experimental results are finally compared.

2. Refined Modeling Strategy

The push-out test is generally a key step in the study of the mechanical response of a steel–concrete composite structure. For this reason, in this section, a refined numerical methodology is proposed for the simulation of such a test. Based on refined "classic" 3D numerical modeling, developments in concrete behavior and connector shear modeling are presented.

2.1. Limits of the "Classical" Simulation of a Push-Out Test

The experimental study proposed in [42] is considered. The ST25-A test is selected from the experimental campaign. It represents the behavior of headed shear studs welded on steel flanges and embedded in concrete blocks. All the characteristics of the components and the methodology of the test follow the recommendations from Eurocode 4 [4] (Figure 3).

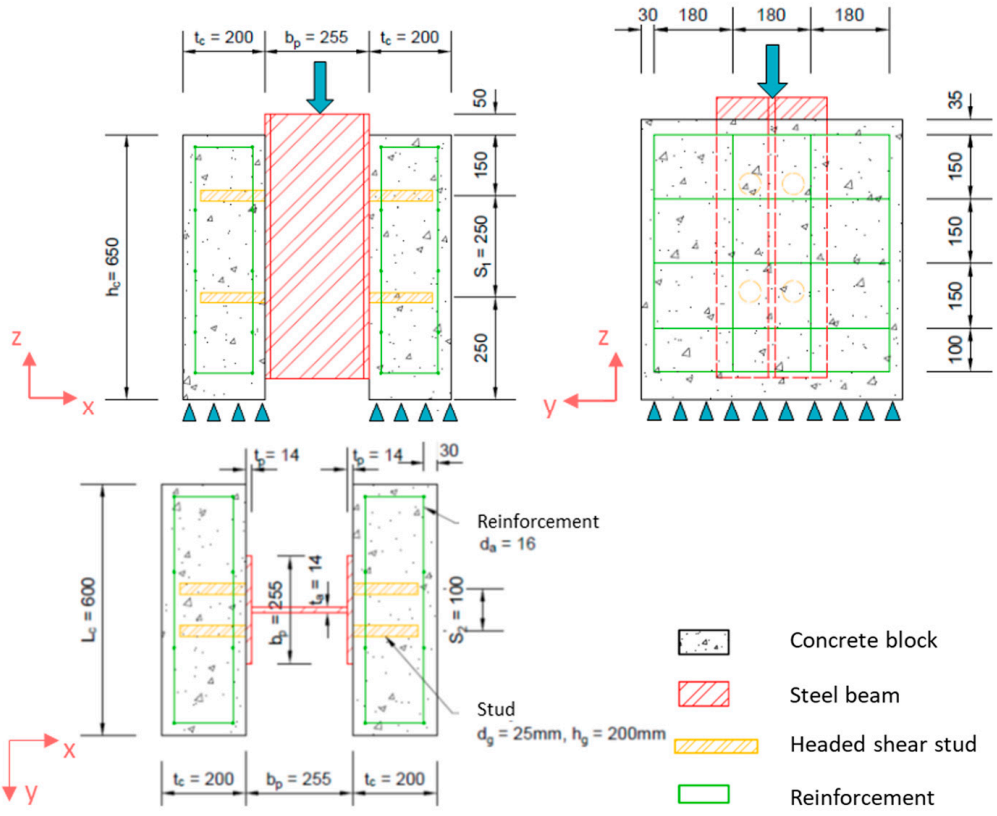

Figure 3. Geometry of a push-out test [42].

The relative slip between the steel beam and the concrete blocks is measured as a function of the applied force. It allows us to define the force P per connector—slip δ behavior law of the connection. The ultimate strength of the connection in shear P_{Rd} (Figure 4a) has been specifically recorded. The experimental failure mode of the specimen is a shear failure of the stud near the welding point with the steel beam (Figure 4b).

Because of the symmetry and considering homogenous material properties in the concrete blocks, only one-fourth of the structure is simulated. The concrete block, the steel

beam, and the connectors are represented by 3D solid elements, while reinforcements are modeled with 1D beam elements. At the interface between the steel connectors and concrete, the nodes related to each material have the same position. The size of the finite element (the cubic root of its volume) ranges from 1.83 mm (in the connectors) to $1d_g$ = 25 mm (away from the connectors) (Figure 5).

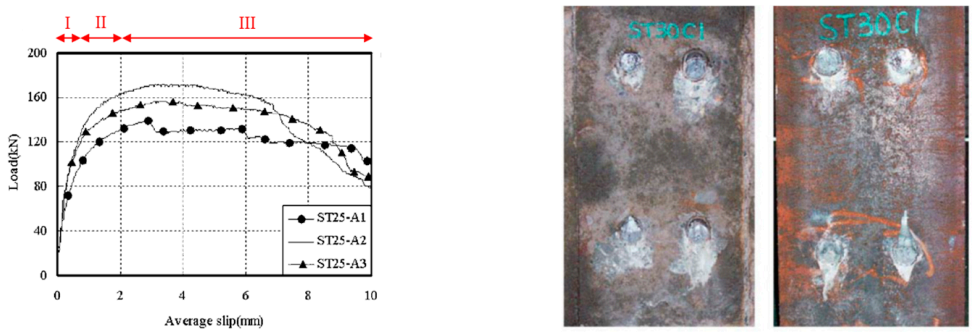

(**a**) (**b**)

Figure 4. (**a**) Force–slip curves of the ST25-A push-out tests. (**b**) Failure pattern of the shear ruin of the stud shank [42].

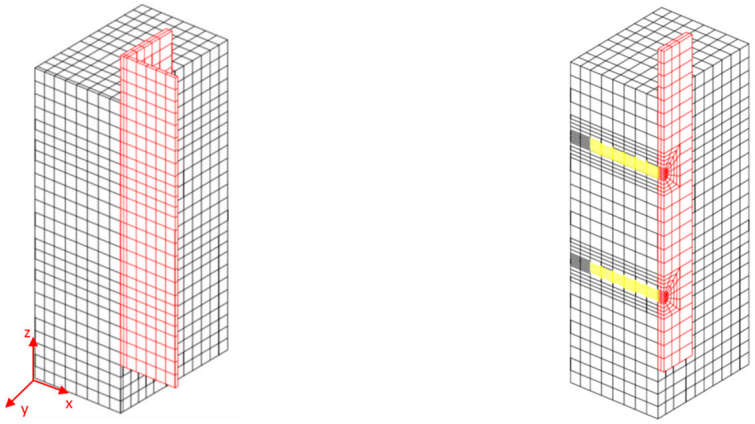

(**a**) (**b**)

Figure 5. Mesh of a quarter the ST25-A push-out test [42], concrete in black, steel beam in red, studs in yellow; (**a**) overall view (**b**) cross section at the stud level.

An isotropic damage model [43] is chosen for the mechanical behavior of concrete blocks. The stress-strain relation is:

$$\sigma_{ij} = (1 - D)C_{ijkl}\varepsilon_{kl} \tag{1}$$

where σ_{ij} and ε_{kl} are the stress and strain components respectively, C_{ijkl} is the fourth order elastic tensor and D is the damage variable. For the description of the damage evolution, an equivalent strain is introduced from the local strain tensor:

$$\varepsilon_{eq} = \sqrt{\sum_{i=1}^{3} (< \varepsilon_i >_+)^2} \tag{2}$$

where $< \varepsilon_i >_+$ are the positive principal strains.

The loading surface g is defined by:

$$g(\varepsilon, D) = \widetilde{d}(\varepsilon) - D \tag{3}$$

where the damage variable D is also the history variable which takes the maximum value reached by $\widetilde{d}$ during the history of loading

$$D = \max\left(\widetilde{d}, 0\right) \tag{4}$$

$\widetilde{d}$ is defined by an evolution law which distinguishes the mechanical responses of the material in tension and in compression by introducing two scalars D_t and D_c

$$\widetilde{d}(\varepsilon) = \alpha_t(\varepsilon) D_t\left(\varepsilon_{eq}\right) + \alpha_c(\varepsilon) D_c\left(\varepsilon_{eq}\right) \tag{5}$$

$$D_t\left(\varepsilon_{eq}\right) = 1 - \frac{\kappa_0}{\varepsilon_{eq}} \exp\left(\frac{l_e . f_{ct}}{G_F}\left(\kappa_0 - \varepsilon_{eq}\right)\right) \tag{6}$$

$$D_c\left(\varepsilon_{eq}\right) = 1 - \frac{\kappa_0(1 - A_c)}{\varepsilon_{eq}} - \frac{A_c}{\exp\left[B_c\left(\varepsilon_{eq} - \kappa_0\right)\right]} \tag{7}$$

$$\alpha_t(\varepsilon) = \left(\sum_{i=1}^{3} \frac{\left\langle \varepsilon_i^t \right\rangle < \varepsilon_i >_+}{\varepsilon_{eq}^2}\right)^{\beta} \tag{8}$$

$$\alpha_c(\varepsilon) = 1 - \alpha_t(\varepsilon) \tag{9}$$

D_t and D_c are the tensile and compressive parts of the damage, respectively. κ_0 is the initial threshold from which damage grows, it is equal to the ratio between the tensile strength f_{ct} and the Young modulus. The weights α_t and α_c are computed from the strain tensor. They are defined as functions of the principal values of the strains ε_i^t and ε_i^c due to positive and negative stresses, respectively. The parameter β reduces the effect of damage under shear compared to tension. A_c and B_c are model parameters characterizing the compression response of the concrete. They are determined to reproduce the compressive strength of the concrete.

Compared to the initial version of the model, for the calculation of D_t (Equation (6)), a Hillerborg energetic method is used to regularize the damage evolution for any element size [33]. This method introduces the dependence of the behavior law on the concrete tension fracture energy G_F and on the element size l_e.

For the steel studs and beams, an elastic–plastic model with an isotropic hardening is chosen. For the reinforcement, an elastic–plastic law without hardening is used. The material parameters are obtained from experimental data [42] (Tables 1–3).

Table 1. Concrete material characteristics [42].

	Value
Compressive strength f_c (MPa)	35.3
Tensile strength f_{ct} (MPa) *	3.23
Young modulus E_c (GPa) *	32.11
Poisson's ratio ν_c (−)	0.2

* Values computed from EC2 [44].

Table 2. Model parameters for the concrete.

G_F $(\mathbf{N.m^{-1}})$	κ_0 (−)	β (−)	A_c (−)	B_c (−)
150	f_{ct}/E_c	1.06	1.55	1900

Table 3. Steel materials characteristics [42].

	Steel Beam	Studs	Reinforcements
Yield limit f_y (MPa)	235	328	500
Young modulus E_s (GPa)	210	213	210
Poisson's ratio ν_s $(-)$	0.3	0.3	0.3
Tangential modulus E_T (GPa)	0.84	0.45	-

The loading and boundary conditions are then defined (Figure 6). First, symmetry conditions are considered on both symmetry faces (zero normal displacements for (conditions a and b)). The concrete block is simply supported on the test set-up, and the vertical displacement is blocked on its bottom face (condition c). A vertical displacement is applied at the top of the steel beam (condition d), and an additional condition is finally imposed on a line at the base of the concrete block to eliminate rigid body movements (condition e).

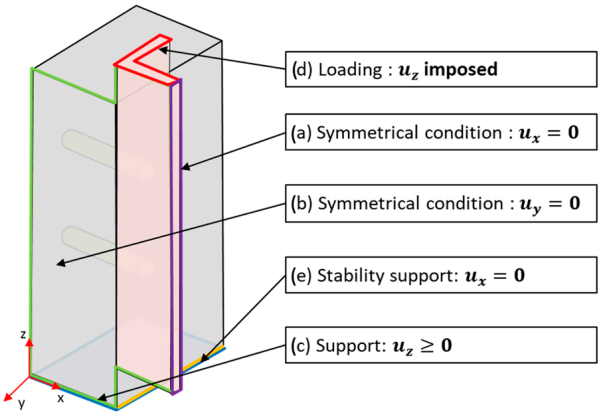

Figure 6. Boundary conditions of the push-out test.

Particular attention must be paid to bonding conditions at the interfaces between components (Figure 7A). First, a perfect bond (same displacement at the interface) is imposed between the concrete and the reinforcement, which plays here a secondary role in the mechanical behavior. A perfect bond is also imposed between the stud heads and the concrete block (condition A, the detailed geometry of the stud heads is not modeled in this study; the bond is imposed on the face at the end of the cylinder) and between the stud feet and the steel beam (condition B). Partial bonds at the interface between the concrete block and the steel beam and between the concrete and the studs are then considered (conditions C and D, respectively). They suppose a contact relation that allows for normal separation and a free slip in the tangential directions. In case of contact, equal displacements are imposed on both materials. In the tangential direction, no friction is considered as the studs are oiled before the test.

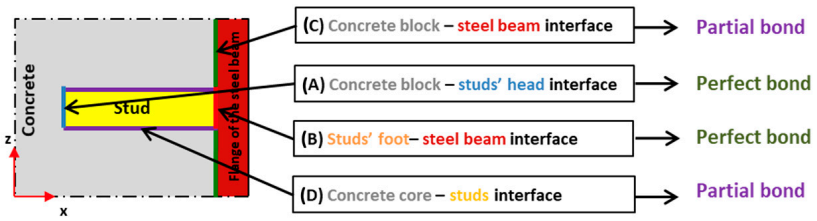

Figure 7. Binding conditions at push-out test interfaces in "classical" modeling.

The simulation is performed using the implicit finite element code Cast3M [45].

The numerical evolution of the load per stud P as a function of the slip δ is illustrated in Figure 8a. A significant difference is noticed in the experimental result. In fact, despite

a similar initial phase, a significant decrease in the numerical stiffness leads to an underestimation of the strength by around 20% compared to the experimental mean strength. After the peak, a brittle failure of the system is simulated. The damage distribution of the concrete, illustrated in Figure 8b, shows an important localization of the damage, which remains concentrated in the concrete elements close to the connectors. In Figure 9, the distribution of the cumulative plastic strain presents a poor yielding of the steel beam and the connectors, which is not in agreement with the experimental observations. In the following sections, improvements are proposed to overcome these two difficulties.

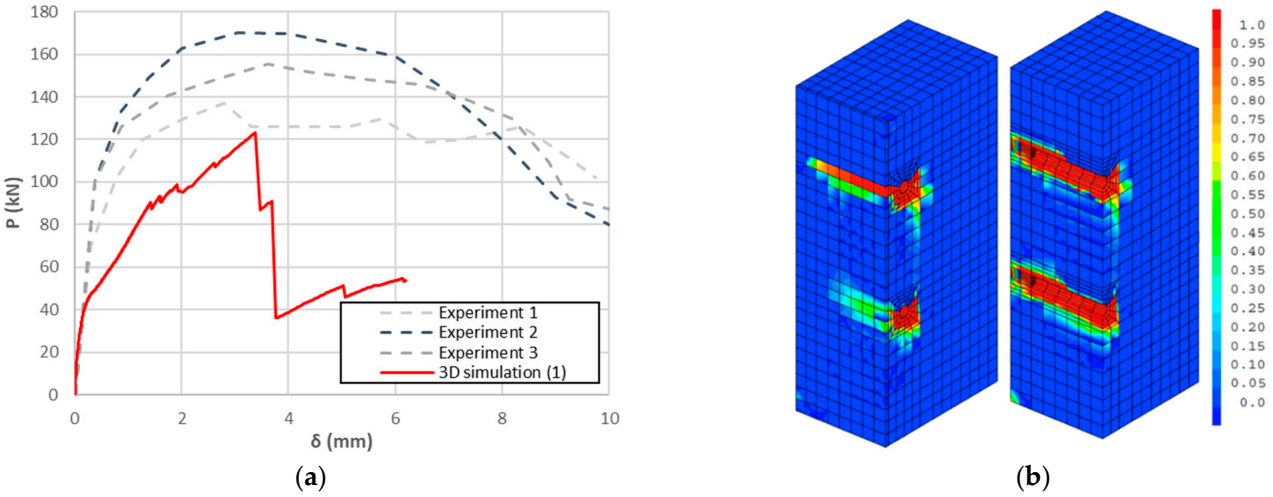

Figure 8. (**a**) Load reduced to a stud–slip of the steel beam curve of the push-out test. (**b**) Final damage distribution in concrete (whole block and cut at the studs) with the "classical" modeling.

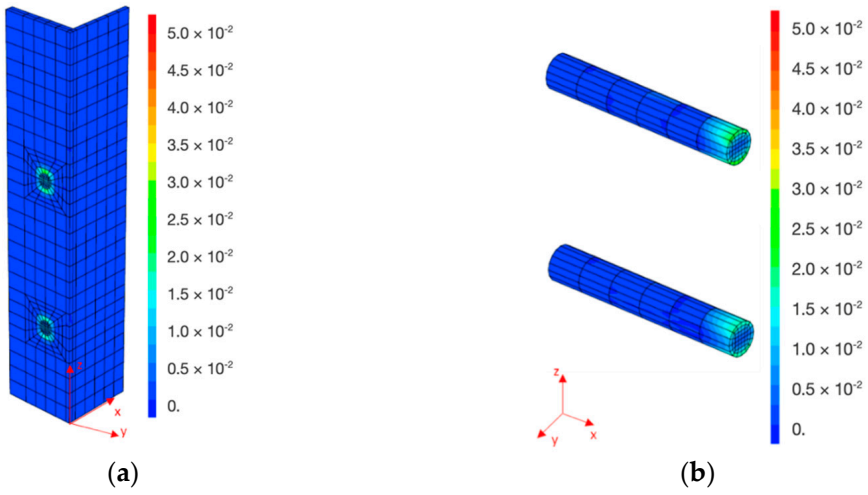

Figure 9. Final plastic strain distribution of (**a**) the steel beam and (**b**) the steel studs for the push-out test with the "classical" modeling.

2.2. Improvement through a Regularization Method in Compression

Because of the highly compressed concrete zones around the connectors, the concrete behavior law needs to be improved. The local description of the mechanical behavior in compression is insufficient, as the stress–displacement evolutions are influenced by the element size. It is thus chosen to adapt the tensile regularization method to the compressive part of the model (D_c). This choice is made from the assumption that in compression, the slenderness of specimens influences the stress–strain curve but not the stress–displacement response, independently of the height of the specimen [36,37,46,47]. This justifies the development of a regularization of the concrete compressive behavior, in which the size of

the finite elements is integrated into the constitutive laws. To do so, from the definition of D_c (Equation (7)), the model parameters A_c and B_c are calibrated from uniaxial compression simulations to obtain the same stress–displacement curves independently on the values of l_e (Figure 10). From this calibration, evolution laws are deduced (polynomial interpolation) for both parameters and applied to the concrete model (Equations (10) and (11)). It is to be noted that this calibration obviously depends on the material properties (compressive strength and softening behavior) and should be recalculated when concrete changes.

$$A_c = -111.91\, l_e^2 + 18.864\, l_e - 0.0017 \tag{10}$$

$$B_c = -310276\, l_e^2 + 31842\, l_e - 2.1143 \tag{11}$$

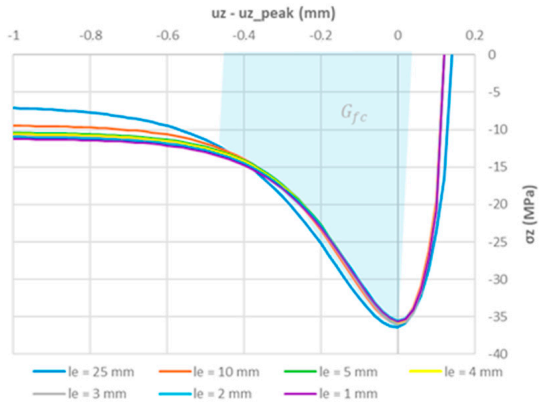

l_e (mm)	A_c (−)	B_c(−)
25	0.4	600
10	0.18	285
5	0.09	150
4	0.072	120
3	0.054	90
2	0.035	60
1	0.0175	30

Figure 10. Stress–displacement curves of concrete cubes in compression of different dimensions with different values of A_c and B_c.

Applied to the push-out test modeling, the global behavior of the system with this new concrete model is illustrated in Figure 11a. A clear improvement is obtained for the load per stud–slip curve. At a slip of $\delta = 3.33$ mm, the numerical load is $P_{num} = 163.4$ kN with a difference of 4.7% with the experimental mean force. The observation of the concrete damage allows for identifying a larger spread (Figure 11b), thus confirming the better distribution of the stress. In addition, several tests have been carried out in [48] and show that the global response is practically independent of the mesh size.

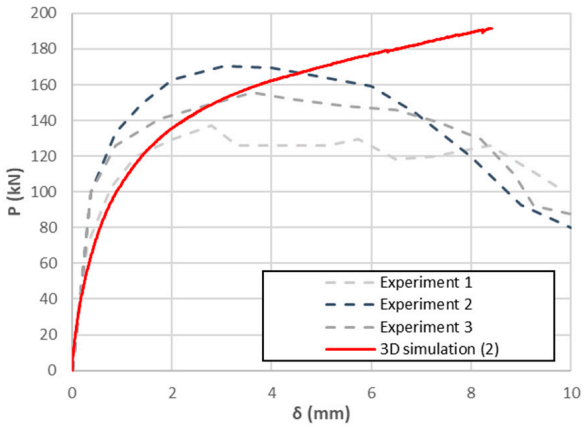

(**a**)

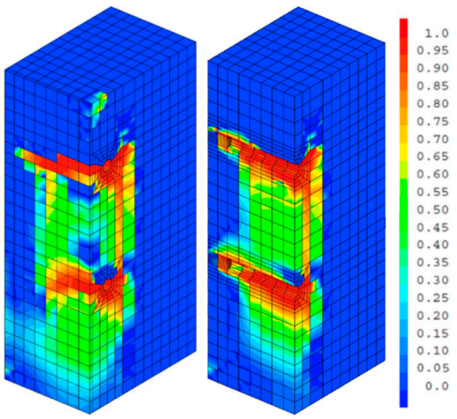

(**b**)

Figure 11. (**a**) Load reduced to a stud–slip of the steel beam curve of the push-out test. (**b**) Final damage distribution in concrete (whole block and cut at the studs) with the new numerical modeling.

For the post-peak behavior, the experimental failure mode is not reproduced numerically, although a shear pattern can be identified in Figure 12. The simulation even provides forces that exceed the shear strength of the push-out test (167 kN) calculated from Equation (12) (from [4] without considering the safety factor), underlining difficulties to reproduce the shear behavior of the steel connectors–steel plates interface.

$$P_{Rd} = \min\left(P_{uc}; P_{ug}\right) = \min\left(0,29\alpha d_g^2\sqrt{f_c E_c}\ ;\ 0,8 A_g f_{ug}\right) \quad (12)$$

2.3. Joint Elements for the Steel Connector–Steel Plate Interfaces

As mentioned in the previous section, the shear behavior at the steel connector–steel plate needs to be improved (condition D in Figure 7). In the push-out test, the most common mode of failure observed experimentally is shearing of the stud near the interface with the steel beam flange. Although this degradation process could be modeled with classical finite element methods, the required spatial discretization would be so fine that it would be inapplicable in terms of numerical cost. For example, an element size of 0.5 mm would be needed to reproduce the pure shear behavior of a single steel bar welded on a steel plate (without concrete) tested in [25], leading to a very large number of elements (Figure 13). With a mesh discretization like the one used in the push-out modeling, an important overestimation of the system strength is visible.

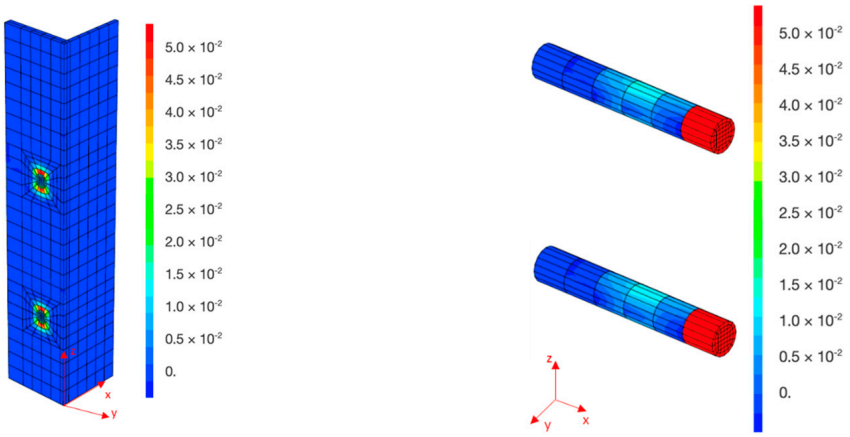

Figure 12. Final plastic strain distribution of (**a**) the steel beam and (**b**) the steel studs for the push-out test with the new numerical modeling.

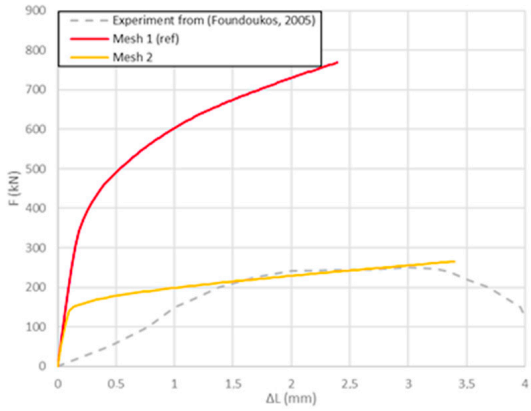

	Maximum elements sizes (mm)			Number of nodes in the mesh
	Direction x (l_x)		Plan yz (l_{yz})	
	Bar	Plate		
Mesh 1 (Ref)	25	7.39	4.9	825
Mesh 2	0.5	0.49	0.49	408,689

Figure 13. Mesh size influence on the shear force–slip curve of the pure shear test on a steel bar welded on a steel plate modeling [25].

To overcome this difficulty, additional junction elements are developed to represent this shear behavior with an acceptable computational cost. They are zero-dimensional spring elements, which connect each node of the stud to the associated node of the steel plate through an orthotropic constitutive law. In the longitudinal direction of the stud (normal to the cross-section), a linear elastic law is supposed. Its stiffness is chosen high enough ($K_n = 10^{12}$ N/m) to reproduce the welding of the stud on the plate. In the tangential directions (respectively, y and z), an elastoplastic law is imposed. The initial stiffness is equal to the normal one, while the plastic criterion is classically written as a function of the force:

$$f(F, X) = \sqrt{\left(F_y - X_y\right)^2 + (F_z - X_z)^2} - P_{ug} \tag{13}$$

with X the hardening parameters in the directions y and z and P_{ug} the shear strength of the steel stud, calculated from EC4 [4] without the safety factor (Equation (14)).

$$P_{ug} = 0.8 f_{ug} A_g \tag{14}$$

where f_{ug} is the ultimate tensile strength of a shear stud and A_g is the stud cross-section. For the hardening parameters, a linear kinematic behavior is supposed through K_{pla} variable. Applied to the push-out test, these junction elements are added at the interface between the studs and the steel beam (condition B in Figure 14). For the plastic behavior, the yield point is determined from Equation (14), $P_{ug} = 167.3$ kN, and the plastic slope is $K_{pla} = 10$ N/m to ensure a quasi-horizontal plateau.

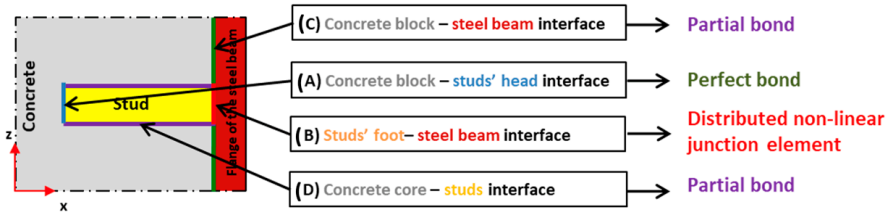

Figure 14. Newinterface binding conditions.

The numerical evolution of the load per stud P as a function of slip δ is illustrated in Figure 15a. Experimental and numerical results agree, and the three major phases of the mechanical behavior are correctly reproduced. The elastic phase (phase I) and the degradation phase (phase II) meet the experimental results, and a horizontal plateau at the shear strength of the stud ($P_{ug} = 167.3$ kN) is finally observed. It is to be noted that the softening behavior is not modeled in the constitutive law of the interface elements. That is why no softening behavior can be numerically obtained. Figure 15b illustrates the damage evolution.

Significant damage is observed under the studs, which characterizes concrete crushing. The cumulative plastic strain distributions of the steel beam and of the steel studs (Figure 16) show shear yielding. Large plastic strains develop at the interface for both elements. These qualitative observations confirm the capacity of the model to reproduce the shear behavior through the junction elements, which leads to a shear failure of the studs in agreement with the experimental observations.

With this refined modeling strategy, several other experimental push-out tests of the literature (different geometries and material characteristics) have been simulated [48]. Numerical results are in good agreement with experimental ones.

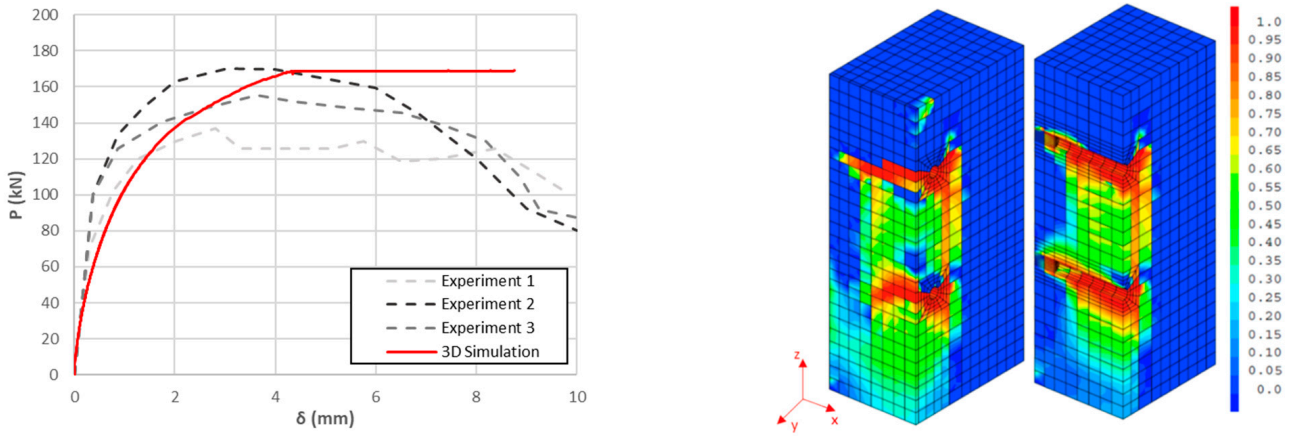

Figure 15. (**a**) Load reduced to a stud–slip of the steel beam curve of the push-out test. (**b**) Final damage distribution in concrete (whole block and cut at the studs) with the proposed modeling.

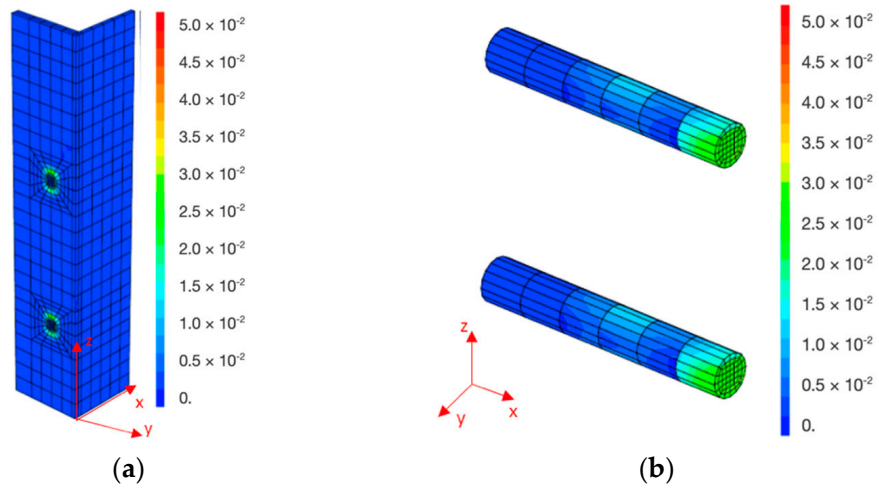

Figure 16. Final plastic strain distribution of (**a**) the steel beam and (**b**) the steel studs for the push-out test with the proposed modeling.

3. Simplified Modeling and Application to SCS Junctions

The numerical modeling strategy that has been previously developed allows us to represent finely the behavior of the composite structure in shear. It has been used to qualify partial or complete composite action in steel–concrete sandwich beams [49]. However, it is numerically costly, both in terms of implementation (mesh generation) and calculation time. It may thus be inapplicable for SCS industrial structures with larger dimensions and complex geometries. A simplified approach is here proposed based on a 1D modeling of the connectors instead of 3D elements. It is validated on the push-out tests and then applied to the mechanical behavior of an SCS junction.

3.1. Simplified Modeling

The representation of the connectors by one-dimensional finite elements anchored in the concrete core aims at easing the mesh discretization, reducing the number of nodes, and finally simplifying the interfacial conditions. The studs are modeled through 1D beam elements. To regularize the behavior and avoid any 1D–3D concentration problems [50], it was decided to locate the 1D elements in the center of the solid concrete elements (3D elements size equal to $1d_g$) (Figure 17).

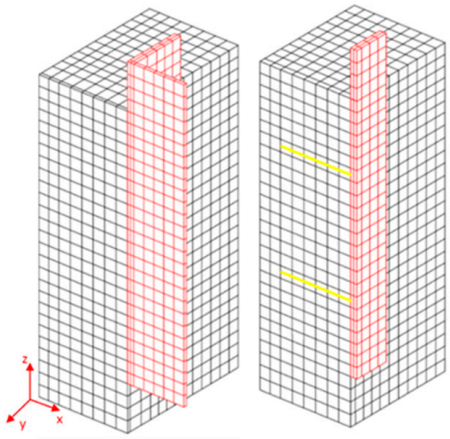

Figure 17. Mesh of a quarter of the ST25-A push-out test [42] modeled with the 1D simplified modeling (overall view and cross section at the stud level); concrete in black, steel beam in red, studs in yellow.

Because of the 1D mesh, no contact can easily be envisaged between the 1D elements of the rod and the 3D elements of the concrete. That is why a perfect bond is considered (the same displacements between the 1D connectors and the concrete elements in which they are embedded). An elastoplastic junction element is still considered to represent the bond between the studs and the steel beam flange (Figure 18, condition D), using the same parameters as the reference methodology.

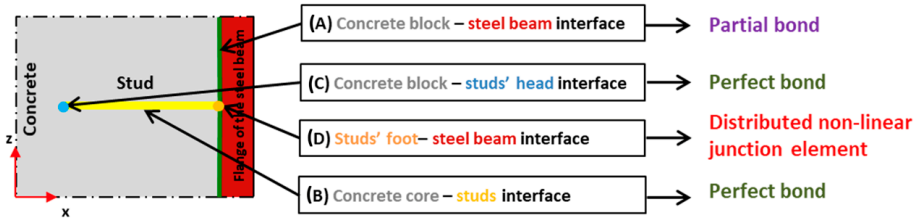

Figure 18. Interface binding conditions of the 1D simplified modeling of the push-out test.

The evolution of the force per stud as a function of the slip of the steel beam is presented in Figure 19. The simplified modeling leads to a higher initial stiffness compared to the reference 3D modeling. It was expected since the contact between the steel studs and concrete had been replaced by a stiffer perfect relation.

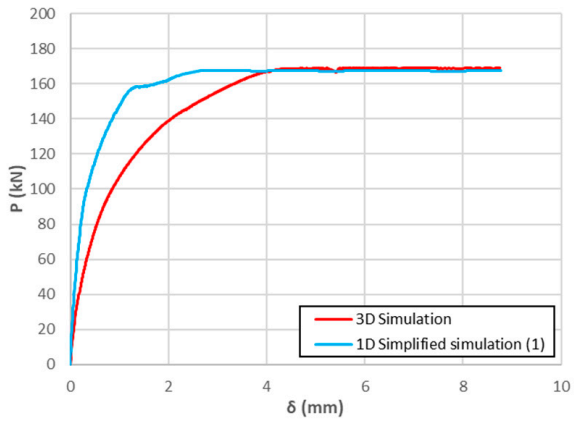

Figure 19. Load reduced to a stud–slip of the steel beam curve of the push-out test.

It is thus proposed to adapt the constitutive law of the junction elements to implicitly consider the push-out behavior, using the theoretical law from [51] between the force and the slip (Equation (15) and Figure 20).

$$P = P_{Rd}\left(1 - \exp\left(-\frac{18}{25.4}\delta\right)\right)^{\frac{2}{5}} \quad (15)$$

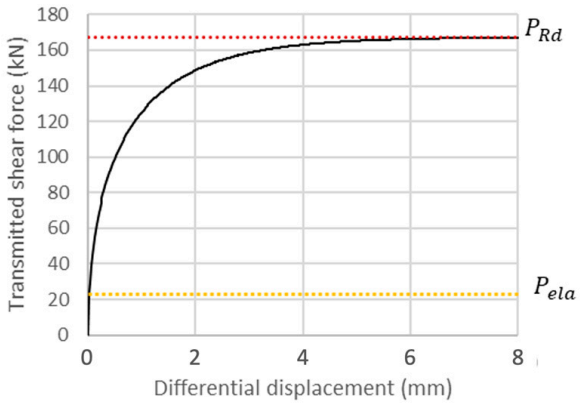

Figure 20. New constitutive law of the shear stud–steel beam junction element system in a tangential direction.

P_{Rd} is the shear strength of the push-out test, defined from the shear failure force of the stud (P_{ug} in Equation (14)) and the failure force of the concrete under the pulling out of the stud P_{uc} [4]:

$$P_{Rd} = \min\left(P_{ug}; P_{uc}\right) = \min\left(0.8 f_{ug} A_g; 0.5 A_g \sqrt{f_c E_c}\right) \quad (16)$$

For the implementation of this elastoplastic behavior, an elastic limit P_{ela} is introduced, calculated from Equation (15) for a slip δ = 0.01 mm, and the strain hardening law follows Equation (15). An illustration of the obtained force–slip function in one tangential direction is illustrated in Figure 20.

The results of the push-out simulation using the new constitutive law for the joint element are shown in Figure 21. The stiffness of the system in the elastic phase is correctly reproduced, as well as the final strength, which corresponds to a shear failure of the studs in Equation (16). As for the reference simulation, the concrete damage initiates near the studs and spreads along the stud shank. However, as expected, due to the 1D simplifications, the simulation fails to represent very local effects (Figure 21b). A drastic decrease in the computational time is obtained (Table 4), validating the ability of the methodology to be applied to industrial applications while remaining representative of the global behavior and the global failure mode.

Table 4. Number of nodes and calculation times of the numerical modeling (on a computer 1 node with 64Go of RAM and 2 Intel Xeon E5-2670 v3 (at 2.30 GHz) and 12 cores per processor).

	Total Number of Nodes	Calculation Times
Refined 3D numerical modeling	7060	8.6 h
Simplified 1D numerical modeling	3850	0.56 h

3.2. Application Example: Junction between SCS Walls

To validate the application of the simplified methodology, it is now directly applied to the study of the mechanical behavior of a steel–concrete–steel junction.

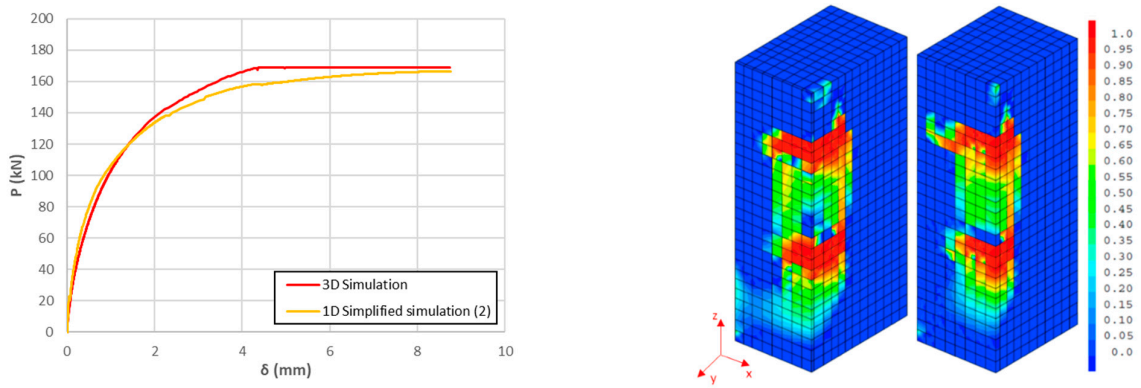

Figure 21. (**a**) Load reduced to a stud–slip of the steel beam curve of the push-out test. (**b**) Final damage distribution in concrete (whole block and cut at the studs) with the new 1D simplified modeling.

3.2.1. Presentation of the Simulation

A wall-to-wall junction experimentally tested as part of the SCIENCE project [52] is modeled. It is a T-intersection that connects a discontinuous SCS wall (thickness $h_{dw} = 0.4$ m) to the center of a continuous SCS wall (thickness $h_{cw} = 0.5$ m). The intersection of the two walls defines the junction area, which is delimited by steel plates connected to the concrete core by head shear studs. The junction connection system consists of headed shear studs and transverse tie rods with a diameter $d_g = 19$ mm. The geometry of the system is illustrated in Figure 22.

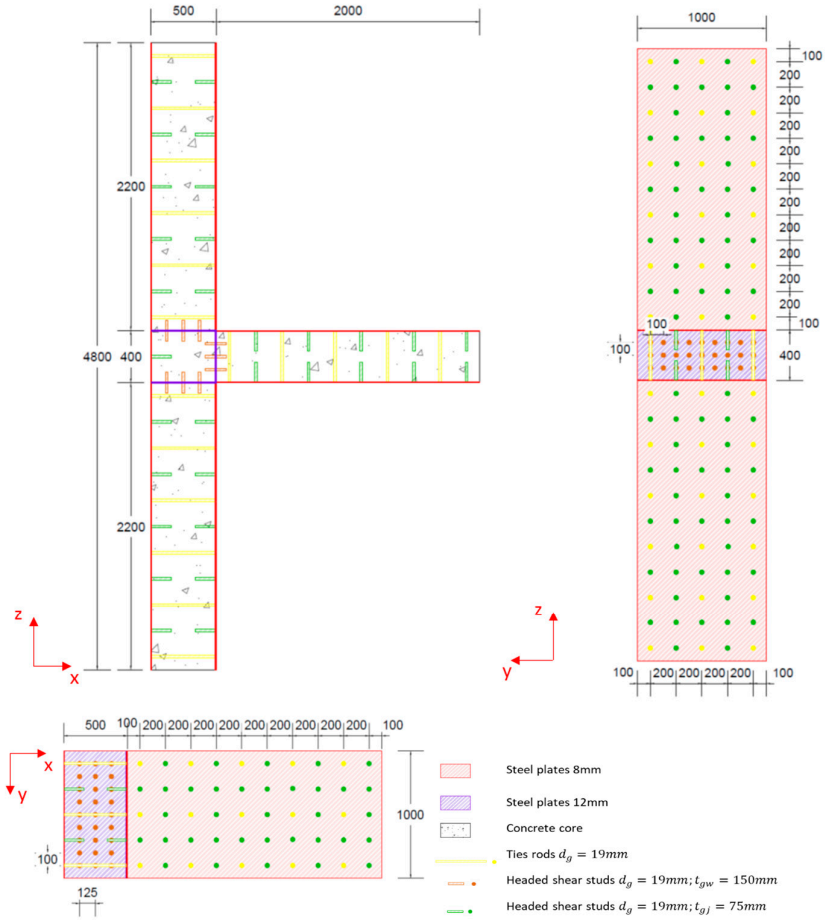

Figure 22. Geometry of the wall-to-wall junction bending test [52].

The concrete core and the steel plates are modeled by 3D solid elements, while the connectors (studs and ties) are modeled by 1D beam elements. Following the simplified strategy, these 1D elements are located at the center of solid concrete elements whose size is equal to $1d_g = 19$ mm. Away from the connectors, the mesh size of the concrete and the steel plates reaches $4d_g$ (Figure 23).

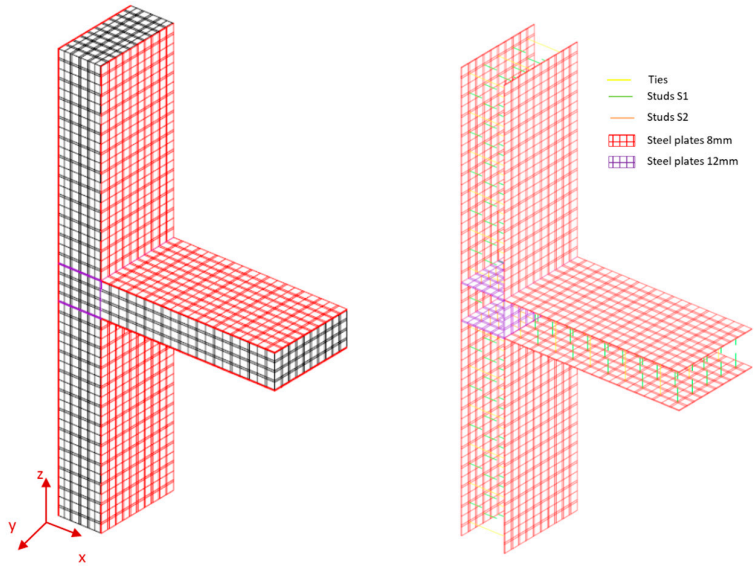

(**a**) (**b**)

Figure 23. Mesh of the studied wall-to-wall junction: (**a**) complete mesh and (**b**) mesh of the steel plates and connectors.

Concrete is modeled using the isotropic damage model, which has been previously discussed, including tensile and compressive regularizations. The parameters are chosen to represent C30/37 concrete. They are calibrated from the material properties and the simulation of uniaxial tension and compression tests for the evolution laws. An elastoplastic model with an isotropic hardening is applied to the steel plates, tie rods and shear studs. The material properties and numerical parameters are summarized in Tables 5–7.

Table 5. Concrete material characteristics from [52].

	Value
Compressive strength f_c (MPa)	37.5
Tensile strength f_{ct} (MPa)	2.8
Young modulus E_c (GPa)	27.6
Poisson's ratio ν_c $(-)$	0.2

Table 6. Model parameters of the concrete core.

G_F $(\mathbf{N.m^{-1}})$	κ_0 $(-)$	β $(-)$	A_c $(-)$	B_c $(-)$
200	f_{ct}/E_c	1.06	$-104.5\, l_e^2 + 27.701\, l_e - 0.0113$	$-221548\, l_e^2 + 34030\, l_e - 9.6231$

The wall-to-wall junction, loaded in bending, is simply supported at both edges of the continuous wall and rests on the test support on one side. The boundary conditions (Figure 24) include blocked displacements in the x direction at the upper and bottom parts (conditions a and b) and in the z direction at the bottom edge (condition c) of the continuous wall. A vertical displacement is imposed on the discontinuous wall (condition d). Condition e reproduces the support of the junction on the test support while ensuring the stability of the system with the displacements blocked in the y direction.

Table 7. Steel material characteristics from [52].

	Wall Plates	Junction Plates	Ties	Studs S1	Studs S2
Yield limit f_y (MPa)	371	408	451	459	499
Young modulus E_s (GPa)	210	210	210	210	210
Poisson's ratio ν_s (−)	0.3	0.3	0.3	0.3	0.3
Hardening modulus E_T (GPa)	0.61	0.56	0.40	0.23	0.24

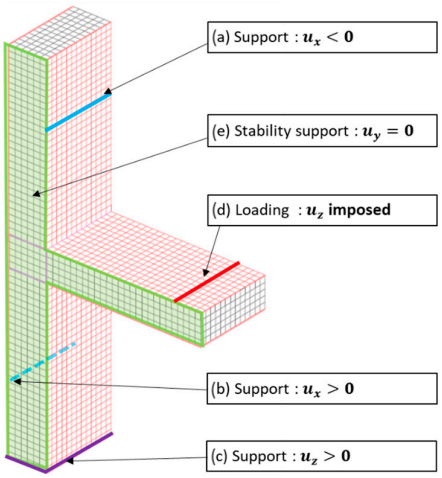

Figure 24. Boundary conditions of the bend test of the SCS wall-to-wall junction.

The bond conditions are the same as for the simplified simulation of the push-out test. For the constitutive law of the joint elements, the shear strengths of the connectors are determined from Equation (16) and summarized in Table 8.

Table 8. Shear strengths of the connectors.

	P_{Rd} (kN)
Ties	128.4
Studs S1 ($h_g = 150$ mm)	113.4
Studs S2 ($h_g = 75$ mm)	123.2

3.2.2. Analysis of the Flexural Behavior

Figure 25a presents the experimental evolutions of the applied load and of the load point displacement as a function of time. Figure 25b illustrates the crack patterns and the failure mode. Several phases can be experimentally identified. First, the opening of a flexural crack in the concrete core of the discontinuous wall ends the initial elastic phase. A progressive loss of stiffness is then observed. It corresponds to the degradation phase with the opening of a diagonal crack in the concrete in the junction and of several cracks in the concrete cores of the connected walls. At a bending load equal to $F = 754$ kN, a peak in the load–time curve characterizes the failure. It is associated with the buckling of the bottom steel plate of the discontinuous SCS wall closed to the junction. Concrete crushing and failure of some tie rods and shear studs due to the instability of the plate complement the failure mode. No additional degradation develops in the junction area, as the design methodology aims at ensuring a junction strength higher than the strongest connected wall.

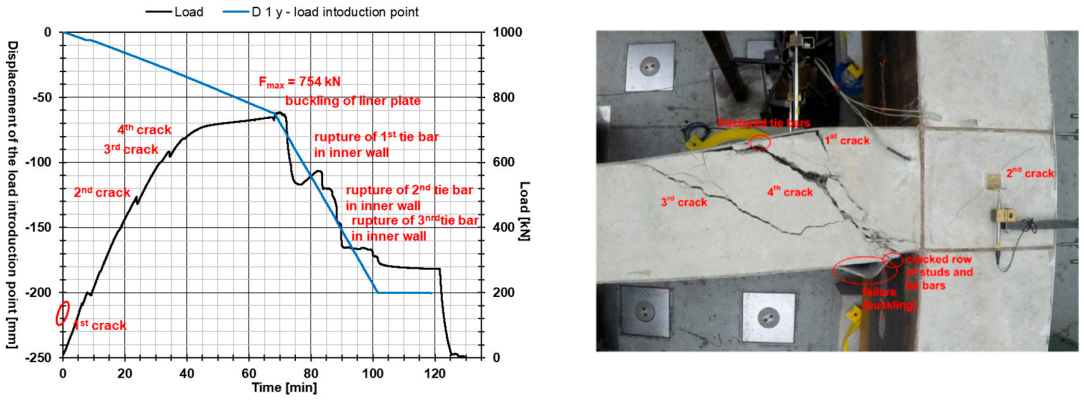

(**a**) (**b**)

Figure 25. (**a**) Applied load–time and displacement of the load point–time curves and (**b**) ruin pattern of the bending test of the SCS junction [52].

Experimental and numerical results are compared in Figure 26. The direct application of the numerical modeling strategy allows us to obtain a good estimation of the mechanical behavior. The different phases are correctly identified (elastic phase until point A and the degradation phase after), even if differences are visible for the initial stiffness. Additional calibration of the model parameters could be investigated, as it is to be noted that the only calibration here is the one from the material properties. Inverse analysis is beyond the scope of the proposed contribution. Moreover, experimental interpretation could explain the observed differences and are currently under investigation (correction of the sensors' values, for example). However, this "blind" application of the simplified methodology is considered promising for simulating the mechanical behavior of complex SCS junctions.

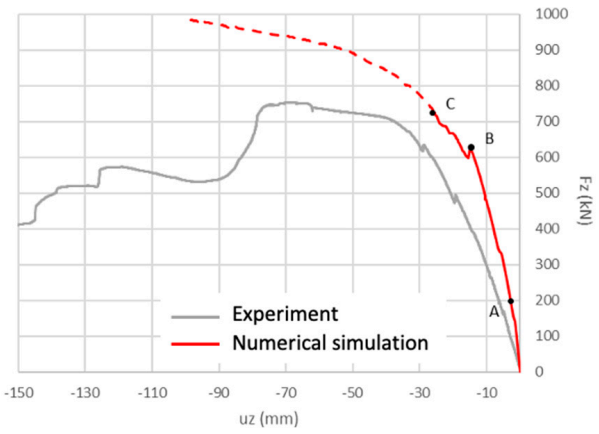

Figure 26. Load–displacement curve of the SCS junction test.

Regarding the failure mode, even if the simulation does not allow us to directly capture the buckling of the compressed plate in the discontinuous wall, it is possible to post-process the stresses in the steel plate and to compare them to the critical buckling resistance σ_c:

$$\sigma_c = \frac{\pi^2 E_s}{\mu^2} = 276.3 \text{ MPa} \tag{17}$$

where E_s is the Young modulus of the steel plate and μ is its slenderness ratio. This parameter is defined as $\mu = L_v/\rho$ with L_v the free length of buckling of the plate ($L_v = 200$ mm equal to the spacing between two rows of studs). ρ is the radius of gyration, $\rho^2 = I_{Gz}/A_{plate}$ with I_{Gz} the inertia moment and A_{plate} the cross-section of the plate. From a vertical displacement of $u_z = -25.5$ mm (point C), the normal stress in the compressed steel plate of

the discontinuous wall is locally higher than the critical buckling strength of the steel. At this displacement, the strength of the system is $F_z = 723.5$ kN with a difference of 4% with the experimental ruin of the system.

Considering the damage distributions (Figure 27), different steps can be identified. The end of the elastic phase corresponds to the opening of the flexural crack in the concrete core of the discontinuous wall (point A). Then, a degradation phase appears with an increase in the concrete damage (flexural crack in the walls) and a decrease in the stiffness of the system (A to C phase). A diagonal crack is also obtained in the junction area at point B. Local degradation around the connectors appears in the walls. However, the number of connectors is sufficient to transfer the stress along the walls. The failure mode of the SCS discontinuous wall is obtained with an inclined shear crack in the concrete core and its extension along the tensile plate of the wall. For the continuous wall, concrete damage develops less and is concentrated around the connectors. In the junction, the damage initiates through the opening of a compression rod. This diagonal crack illustrates the shear forces in the concrete inside the joint.

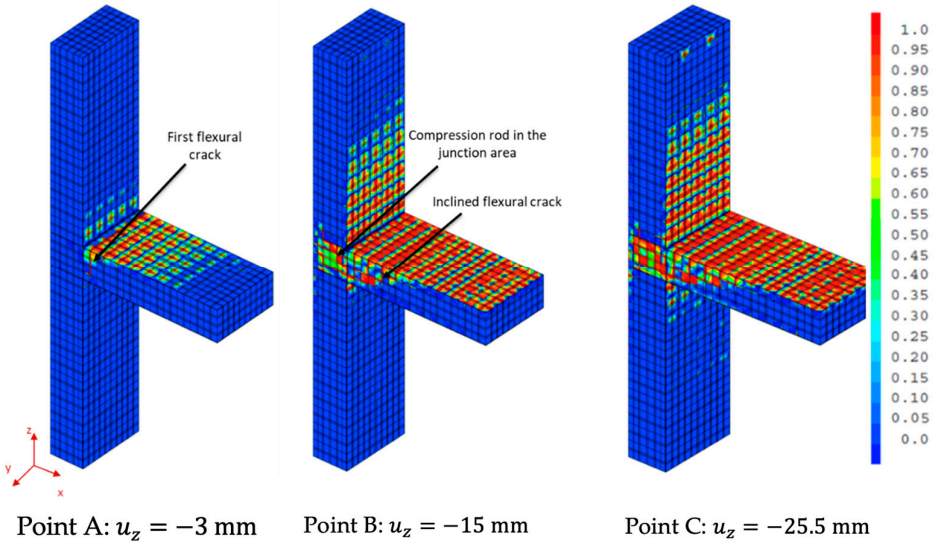

Figure 27. Damage patterns of the concrete of the SCS junction in bending.

Figures 28 and 29 show the equivalent von Mises stresses inside steel components (connectors and steel plates). Significant stresses are observed in the studs and the ties in the discontinuous wall close to the welding with the steel plates. The yielding of some ties crossing a concrete shear crack is also noticed. It confirms the participation of the connectors. For the steel plates, significant yield stresses developed close to the junction for both continuous and discontinuous walls. Yielding of the tensile plate of the discontinuous wall is simulated in agreement with the experimental results.

Finally, even if the experimental ruin of the test is due to the failure of the discontinuous wall, the observations of the mechanical behaviors of each component also enable us to identify the critical points of the junction. These areas correspond to the ones that develop the higher stresses. In our case, the steel plates close to the junction develop significant stresses, as well as the concrete of the loaded wall. The large number of connectors allows for distributing the shear stresses, which develop against the slip between the concrete cores and the steel plates. It thus ensures the full composite action. The most loaded components of the junction zone are the plates at the corner and the concrete core, which work according to the compression rod principle. The studs within this zone are impacted by significant shear and tensile stresses to avoid the separation of the steel plates and the concrete core. Special care should be paid to these elements for the design and the analysis of the response of SCS wall-to-wall junctions.

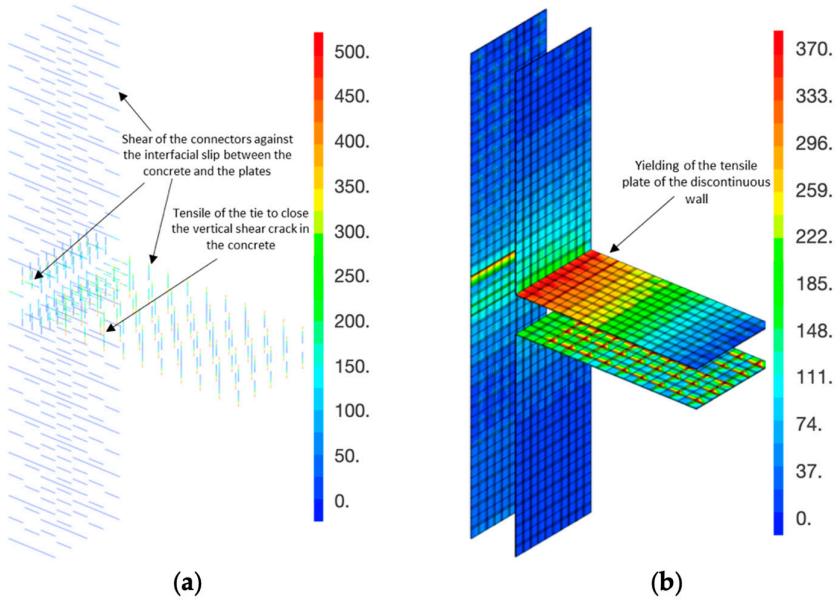

Figure 28. Equivalent von Mises stresses (in MPa) at loading point C (**a**) for the connectors and (**b**) for 8 mm thick steel plates.

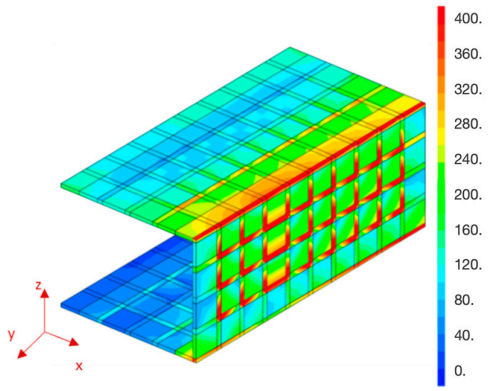

Figure 29. Equivalent von Mises stresses (in MPa) at loading point C for 12 mm thick steel plates.

4. Conclusions

Steel–concrete–steel composite structures are competitive choices in the construction field. Their high resistance, stiffness, sustainability, and modularity support their use in new high buildings, blast and impact shield walls, submerged tunnels, or nuclear power plants. To get a better understanding of their complex composite behaviors, an adapted modeling strategy is proposed in this contribution.

The local shear behavior of the connection system was first investigated through the simulation of a push-out test using refined 3D modeling. To reproduce the experimental behavior, two improvements were proposed compared to classical finite element simulations. First, compressive regularization was introduced in the concrete constitutive law, with the definition of evolution laws for the model parameters as a function of the element size. Then, elastoplastic junction elements at the interface between stud and plate were developed. They both ensured an appropriate simulation of the mechanical response (global and local behaviors).

However, for simulating the behavior of large structures, the refined strategy would be too costly in terms of memory and computing time. Based on the refined modeling strategy, simplifications were proposed, considering studs as 1D beam elements. The constitutive law of the junction element was modified to account for the consequences of local effects,

which cannot be reproduced by 1D elements. This simplified strategy was successfully applied to the push-out test as a validation.

Finally, this simplified modeling strategy was applied to an SCS wall-to-wall junction. Despite some differences with the experimental results, this simulation was able to reproduce the global response of the system. The degradation process was correctly captured, and critical zones can be identified as the most likely to fail. For the studied wall-to-wall junction, these points correspond to the areas of the connected wall close to the junction and, the corner zone of the plate, and the concrete core of the junction.

The compression regularization method presented in this article is somewhat tedious, as it requires the coefficients of Mazars' law in compression to be identified for different element sizes. Developments are underway to propose a modification of the law so that cracking energy is explicitly included in the equations as for tension. At the structure level, additional studies could be launched with special care on critical zones to improve the knowledge and better predict the behavior of structures. A "multilevel strategy" between refined and simplified methodologies could be an option to reach this goal.

The proposed refined modeling is reliable for understanding local degradation phenomena around studs and for conducting parametric studies and avoiding costly tests, for example, on the relative size of studs and plates. The proposed simplified strategy, less demanding in terms of calculation time but relatively reliable, enables parametric simulations on the scale of structural elements (beams, walls, junctions, etc.) to study, for example, the influence of the spatial distribution of studs or the presence of defects, which would be costly if exhaustive experimental tests were carried out.

Author Contributions: Conceptualization, L.D. and L.J.; methodology, L.D. and L.J.; software, R.C.; validation, L.D., L.J. and R.C.; investigation, R.C.; writing—original draft preparation, R.C.; writing—review and editing, L.D.; supervision, L.D. and L.J.; project administration, L.J.; funding acquisition, L.J. All authors have read and agreed to the published version of the manuscript.

Funding: The project was funded by EDF R & D and CEA, tripartite institute agreement number 2020-F35158.

Data Availability Statement: The data presented in this study are available in the article.

Acknowledgments: The authors gratefully acknowledge the partial financial support from EDF R & D for the development and analysis of the simulation results.

Conflicts of Interest: The authors declare no conflict of interest. The funders had no role in the design of the study; in the collection, analyses, or interpretation of data; in the writing of the manuscript; or in the decision to publish the results.

References

1. Montague, P. A simple Composite Construction for cylindrical shells subjected to external pressure. *J. Mech. Eng. Sci.* **1975**, *17*, 105–113. [CrossRef]
2. Solomon, S.K.; Smith, S.; Cursens, A. Flexural tests of steel-concrete-steel sandwiches. *Mag. Concr. Res.* **1976**, *28*, 13–20. [CrossRef]
3. Wright, H.; Oduyemi, T.; Evans, H. The experimental behavior of double skin composite elements. *J. Construct. Steel Res.* **1991**, *19*, 97–110. [CrossRef]
4. *EN 1994-1-1:2004*; CEN Eurocode 4: Design of Composite Steel and Concrete Structures—Part 1-1: General Rules for Buildings—European Standard. European Committee for Standardization: Brussels, Belgium, 2004.
5. Roberts, T.; Edwards, D.; Narayanan, R. Testing and Analysis of Steel-Concrete-Steel Sandwich Beams. *J. Construct. Steel Res.* **1996**, *38*, 257–279. [CrossRef]
6. Bowerman, H.; Coyle, N.; Chapman, J. An innovative steel-concrete construction system. *Struct. Eng.* **2002**, *80*, 33–38.
7. Liew, J.R.; Sohel, K. Lightweight steel-concrete-steel sandwich system with J-hook connectors. *Eng. Struct.* **2009**, *31*, 1166–1178. [CrossRef]
8. Zhang, W.; Huang, Z.; Fu, Z.; Qian, X.; Zhou, Y.; Sui, L. Shear resistance behavior of partially composite Steel-Concrete-Steel sandwich beams considering bond-slip effect. *Eng. Struct.* **2020**, *210*, 110394. [CrossRef]
9. Oduyemi, T.; Wright, H. An Experimental Investigation into the Behaviour of Double-Skin Sandwich Beams. *J. Construct. Steel Res.* **1989**, *14*, 197–220. [CrossRef]
10. Booth, P.N.; Varma, A.H.; Sener, K.C.; Malushte, S.R. Flexural behavior and design of steel-plate composite (SC) walls for accident thermal loading. *Nucl. Eng. Des.* **2015**, *295*, 817–828. [CrossRef]

11. Bowerman, H.; Pryer, J. Advantages of British steel bi-steel in immersed tunnel construction. In Proceedings of the IABSE Colloquim—Tunnel Structures, Stockholm, Sweden, 4–6 June 1998; IABSE Reports: 78. IABSE: Zurich, Switzerland, 2015.
12. Yan, J.-B.; Liew, J.R.; Zhang, M.-H.; Sohel, K. Experimental and analytical study on ultimate strength behavior of steel-concrete-steel sandwich composite beam structures. *Mater. Struct.* **2015**, *48*, 1523–1544. [CrossRef]
13. Varma, A.H.; Malushte, S.R.; Lai, Z. Modularity & Innovation using steel-plate composite (SC) walls for nuclear and commercial construction. In Proceedings of the 11th International Conference: Advances in Steel-Concrete Composite Structures (ASCCS), Beijing, China, 3–5 December 2015.
14. Leekitwattana, M.; Boyd, S.; Shenoi, R. An alternative design of steel-concrete-steel sandwich beam. In Proceedings of the 9th International Conference on Sandwich Structures (ICSS 9), Pasadena, CA, USA, 13–15 June 2010.
15. *MPR-2610*; Application of Advanced Construction Technologies to New Nuclear Power Plants. US Department of Energy: Washington, DC, USA, 2004.
16. AISC 2017. Available online: https://www.aisc.org/pressreleases/press-releases/steel-core-system-revolutionizes-high-rise-construction/ (accessed on 31 August 2023).
17. Calatrava. 2013. Available online: https://calatrava.com/projects/sharq-crossing-doha.html (accessed on 31 August 2023).
18. Bekarlar, K. Steel-Concrete-Steel Sandwich Immersed Tunnels for Large Spans. Master's Thesis, Delft University of Technology, Delft, The Netherlands, 2016.
19. Liew, J.R.; Yan, J.-B.; Huang, Z.-Y. Steel-concrete-steel sandwich composite structures—Recent innovations. *J. Construct. Steel Res.* **2017**, *130*, 202–221. [CrossRef]
20. WEC, 2021. Westingthouse Electric Company—AP1000-PWR. Available online: https://www.westinghousenuclear.com/new-plants/ap1000-pwr (accessed on 31 August 2023).
21. MHI, 2013. Mitsubishi Heavy Industry—Advanced OWR, IEAE INPRO 7th Dialogue Forum. Available online: https://nucleus.iaea.org/sites/INPRO/df7/Session%202/Vendor%201/03Mitsubishi_Handout_MHI_DF7_Description_US-APWR.pdf (accessed on 31 August 2023).
22. Lohani, V. Effects of Geometric and Material Parameters on Failure Modes of SC Elements. Master's Thesis, Aalto University, Espoo, Finland, 2016.
23. Seo, J.; Varma, A.H. Steel-Plate Composite Wall-to-Wall T-Joints: Joint Shear Strength. *J. Struct. Eng.* **2019**, *145*, 04019054. [CrossRef]
24. Sener, K.C.; Varma, A.H.; Seo, J. Experimental and numerical investigation of the shear behavior of steel-plate composite (SC) beams without shear reinforcement. *Eng. Struct.* **2016**, *127*, 495–509. [CrossRef]
25. Foundoukos, N. Behaviour and Design of Steel Concrete Steel Sandwich Construction. Ph.D. Thesis, Imperial College of Science, London, UK, 2005.
26. Nguyen, Q.-N. Modélisation du Comportement Non-Linéaire des Poutres Mixtes Acier-Béton avec Prise en Compte des Effets Différés. Ph.D. Thesis, Institut National des Sciences Appliquées de Rennes (INSA), Rennes, France, 2009. (In French).
27. Bujnak, J. Analyse Globale de Poutres Mixtes Acier Béton: Approche Analytique et Modélisation Non Linéaire. Ph.D. Thesis, University Blaise Pascal, Clermont Ferrand, France, 2007. (In French).
28. Bouchair, A.; Bujnak, J.; Duratna, P.; Lachal, A. Modeling of steel-concrete push-out test. *Procedia Eng.* **2012**, *40*, 102–117. [CrossRef]
29. Yan, J.-B.; Zhang, W. Numerical analysis on steel-concrete-steel sandwich plates by damage plasticity model: From materials to structures. *Constr. Build. Mater.* **2017**, *149*, 801–815. [CrossRef]
30. Yan, J.-B.; Zhang, W.; Liew, J.Y.R.; Li, Z.-X. Numerical studies on shear resistance of headed stud connectors in different concretes under Arctic low temperature. *Mater. Des.* **2016**, *112*, 184–196. [CrossRef]
31. Xie, M.; Foundoukos, N.; Chapman, J. Experimental and numerical investigation on the shear behaviour of friction-welded bar-plate connections embedded in concrete. *J. Constr. Steel Res.* **2004**, *61*, 625–649. [CrossRef]
32. Qureshi, J.; Lam, D. Behaviour of Headed Shear Stud in Composite Beams with Profiled Metal Decking. *Adv. Struct. Eng.* **2012**, *15*, 1547–1558. [CrossRef]
33. Hillerborg, A.; Modéer, M.; Peterson, P.-E. Analysis of crack formation and crack growth in concrete by means of fracture mechanics and finite elements. *Cem. Concr. Res.* **1976**, *6*, 773–792. [CrossRef]
34. Pijaudier-Cabot, G.; Mazars, J.; Pulikowski, J. Steel-Concrete Bond Analysis with Nonlocal Continuous Damage. *J. Struct. Eng.* **1991**, *117*, 862–882. [CrossRef]
35. Chambon, C.; Caillerie, D.; Matsuchima, T. Plastic continuum with microstructure, local second gradient theories for geomaterials: Localization studies. *Int. J. Solids Struct.* **2001**, *38*, 8503–8527. [CrossRef]
36. Van Mier, J. Strain-Softening of Concrete under Multiaxial Loading Condition. Ph.D. Thesis, Technische Hogeschool, Eindhoven, The Netherlands, 1984.
37. Jansen, D.C.; Shah, S.P. Effect of length on compressive strain softening of concrete. *J. Eng. Mech.* **1997**, *123*, 25–35. [CrossRef]
38. Nakamura, H.; Higai, T. Compressive fracture energy and fracture zone length of concrete. In *Modeling of Inelastic Behavior of RC Structures Under Seismic Loads*; Shing, P., Tanabe, T., Eds.; ASCE: Reston, VA, USA, 2001.
39. D'Ottavio, M.; Krasnobrizha, A.; Valot, E.; Polit, O.; Vescovini, R.; Dozio, L. Dynamic response of viscoelastic multiple-core sandwich structures. *J. Sound Vib.* **2021**, *491*, 115753. [CrossRef]

40. Rezaiee-Pajand, M.; Masoodi, A.R.; Mokhtari, M. Static analysis of functionally graded non-prismatic sandwich beams. *Adv. Comput. Des.* **2018**, *3*, 165–190.
41. Rezaiee-Pajand, M.; Arabi, E.; Masoodi, A.R. Nonlinear analysis of FG-sandwich plates and shells. *Aerosp. Sci. Technol.* **2019**, *87*, 178–189. [CrossRef]
42. Shim, C.S.; Lee, P.-G.; Yoon, T.Y. Static behavior of large stud shear connectors. *Eng. Struct.* **2004**, *26*, 1853–1860. [CrossRef]
43. Mazars, J. Application de la Mécanique de l'Endommagement au Comportement non Linéaire et à la Rupture du Béton de Structure. Ph.D. Thesis, Université Pierre et Marie Curie, Paris, France, 1984. (In French).
44. *EN 1992-1-1: 2004*; CEN Eurocode 2. Design of Concrete Structures—Part 1-1: General Rules for Buildings—European Standard. European Committee for Standardization: Brussels, Belgium, 2004.
45. CEA, 2021. Cast3M. Available online: http://www-cast3m.cea.fr (accessed on 31 August 2023).
46. Markeset, G. Failure of Concrete under Compressive Strain Gradients. Ph.D. Thesis, University of Trondheim, Trondheim, Norway, 1993.
47. Rokugo, K.; Koyanagi, W. Role of compressive fracture energy of concrete on the failure behavior of reinforced concrete beams. In *Applications of Fracture Mechanics to Reinforced Concrete*, 1st ed.; Carpinteri, A., Ed.; CRC Press: London, UK, 1992.
48. Calixte, R. Simulation du Comportement de Structures "Steel-Concrete-Steel" sous Chargement Mécanique. Ph.D. Thesis, Paris Nanterre University, Nanterre, France, 2021. (In French).
49. Calixte, R.; Jason, L.; Davenne, L. Partial to Full Composite Action in Steel–Concrete Sandwich Beams: Development of a Modeling Strategy and Comparison to Standards. *Int. J. Civ. Eng.* **2022**, *20*, 1327–1342. [CrossRef]
50. Llau, A.; Jason, L.; Dufour, F.; Baroth, J. Finite Element modelling of 1D inclusions in 3D domains: Application to steel components in concrete structures. *Eng. Struct.* **2016**, *127*, 769–783. [CrossRef]
51. Ollgaard, J.; Slutter, R.; Fisher, J. Shear strength of stud connectors in lightweight and normal-weight concrete. *AISC Eng. J.* **1971**, *71–10*, 55–64.
52. Burgan, B.A.; Aggelopoulos, E.S.; Chryssanthopoulos, M.K.; Sagaseta, J.; Francis, P.; Fülöp, L.; Lohani, V.; Herrmann, N.; Muller, M.; Tuscher, J.L.; et al. *SC for Industrial, Energy and Nuclear Construction Efficiency: Final Report*; EU Publications, EUR 28912; Publications Office of the European Union: Luxembourg, Luxembourg, 2017.